Vietnam Journal of Mechanics, Vol. 48, No. 2 (2026), pp. 141 – 160
DOI: https://doi.org/10.15625/0866-7136/23589

A SYMMETRIC ROBERTS-BASED COMPLIANT MECHANISM FOR POTENTIAL APPLICATION IN A HIGH-FREQUENCY FAST TOOL SERVO SYSTEM

Tan Thang Nguyen[1], **Thanh-Phong Dao**[1], **Hieu Giang Le**[1], **Nhat Linh Ho**[2,*]
[1]*Faculty of Mechanical Engineering, Ho Chi Minh City University of Technology and Engineering, Ho Chi Minh City, Vietnam*
[2]*Institute of Engineering, HUTECH University, Ho Chi Minh City, Vietnam*
E-mail: hn.linh@hutech.edu.vn

Received: 5 October 2025 / Revised: 10 December 2025 / Accepted: 20 January 2026
Published online: 8 June 2026

Abstract. The primary objective of this paper is to present the design and analysis of a symmetric, fully compliant linear-motion mechanism based on Roberts linkages for potential application in high-frequency fast tool servo systems used in ultra-precision machining. The proposed structure employs a four-branch symmetric configuration that provides highly accurate translational guidance, significantly reduces parasitic motion, and enhances stiffness uniformity within a compact monolithic structure. Analytical modeling using the pseudo-rigid-body method and Lagrangian formulation was conducted to derive the stiffness and dynamic characteristics, and the results were validated through finite element analysis. The comparison showed good agreement, with deviations of 15.72% in stiffness and 10.10% in natural frequency. Static evaluation confirms a highly linear force–displacement response with exceptionally low parasitic motion ($< 0.02\%$) and a maximum stress of only 8.5 MPa, well below the yield strength of Al7075. The first natural frequency of 1289 Hz suggests that the mechanism may be suitable for high-bandwidth FTS applications. Owing to its high stiffness, low parasitic error, and superior dynamic performance, the proposed compliant linear guide represents a promising solution for next-generation fast tool servo systems in ultra-precision diamond turning.

Keywords: ultra-precision, fast tool servo systems, compliant mechanisms, Roberts mechanism, pseudo-rigid-body model.

1. INTRODUCTION

Ultra-precision diamond turning has become a key manufacturing technology for producing freeform optics, microstructure surfaces, and high-accuracy components, owing to its capability to achieve nanometric surface finishes and sub-micrometer form accuracy (Abdulkadir et al., 2018; Cheung & Lee, 2000; Mishra et al., 2019). To meet the rising demand for machining complex surfaces, fast tool servo (FTS) systems have been increasingly integrated into ultra-precision lathes. These lathes operate on the principle of combining high-frequency FTS operation with sub-micrometer positioning accuracy, allowing the tool to track complex surface profiles in real time (Tian et al., 2015; To et al., 2006; Yang & Zhu, 2020; L. Zhu et al., 2018).

Traditionally, most FTS units employ assembly-based structures in which a piezoelectric actuator (PZT) drives a motion guidance system consisting of rigid mechanical guides combined with amplifiers. While such hybrid designs can deliver acceptable stroke and stiffness, their reliance on sliding or rolling elements inevitably introduces friction, backlash, wear, and

geometric hysteresis. These factors deteriorate motion repeatability, reduce dynamic bandwidth, and negatively affect long-term stability during high-frequency machining (Tian et al., 2016; Wang et al., 2018).

To overcome these limitations, fully compliant mechanisms have attracted considerable attention for FTS applications. By generating motion entirely through elastic deformation, fully compliant mechanisms completely eliminate mechanical couplings and thus ensure frictionless, backlash-free operation with excellent repeatability and structural integrity (Howell, 2001). However, existing fully compliant FTS mechanisms still have several inherent limitations. First, many designs still suffer from high parasitic motion. Second, to ensure high-frequency feedback performance of fast servo tools, the natural frequency of the flexure-hinge tool holder should be greater than 1000 Hz (Z. Li et al., 2021). However, most FTS mechanisms have low natural frequencies (200–800 Hz) (H. Li et al., 2021; Liang et al., 2017; Ma et al., 2013), which limits their application under a wide range of cutting conditions at wide bandwidth. Third, most compliant designs are based on parallel-guide mechanisms that use only one or two compliant beams, thereby limiting the guidance accuracy and load capacity (W. Chen, Shi, et al., 2013a; Hubbard et al., 2004; Liang et al., 2017; Yong, 2020; Z. Zhu et al., 2020).

In recent years, Wan et al. (2016), W. Chen, Jiang, Liu, et al. (2013), and W. Chen, Shi, et al. (2013a) have used compliant Roberts linear guides in micro-positioning stages, force sensors, and compliant grippers, respectively, because these guides can approximate linear motion better than conventional parallel guides, as shown by Hubbard et al. (2004). However, the compliant Roberts straight-line mechanism in Wan et al. (2016) is typically optimized for low-frequency operation, and its structural configuration does not fully meet the demanding high-bandwidth requirements of fast tool servo systems. To date, no research has investigated the application of a multi-branch, symmetric, fully compliant Roberts-based structure specifically designed for the dual goals of high dynamic stiffness and minimal parasitic motion in a compact FTS design.

Motivated by these gaps, this study proposes a new fully compliant planar linear-motion mechanism specifically designed for high-bandwidth fast tool servo applications. The contributions of this research can be summarized as follows:

- A four-branch symmetric compliant structure: unlike the existing FTS mechanisms reported by Paniselvam et al. (2023), which use one or two parallel guide mechanism modules, the proposed configuration integrates four compliant Roberts linkages arranged symmetrically. This multi-branch structure significantly enhances motion linearity, suppresses parasitic rotation, and ensures uniform stiffness distribution across the mechanism.

- High stiffness-to-footprint performance suitable for high-bandwidth operation: with an overall size of $70.8 \times 63 \times 10$ mm, the mechanism achieves a first natural frequency of 1289.3 Hz, enabling a wide safe operating bandwidth and reducing susceptibility to resonance during high-frequency cutting.

- Low parasitic motion tailored for FTS cutting-load conditions: the mechanism maintains parasitic motion below 0.02%, substantially lower than typical compliant FTS systems. The symmetric design also improves stability under axial cutting forces, an essential requirement for diamond turning.

To analyze the behavior of the FTS, the PRBM and the Lagrange equation are used as effective computational tools in the field of elastic mechanisms. Although the PRBM has been applied to many compliant structures, its application to the construction and validation of the model for a four-arm FTS mechanism is also valuable for modeling. The analytical predictions are systematically compared with the FEA results to verify the stiffness, stress distribution, and modal behavior.

To make the structure of the study clear, the paper is organized as follows. Section 2 explains the conceptual design of the mechanism, including its structure and working principle. Section 3 introduces the finite element modeling process, describing the meshing method, boundary

conditions, and the procedures for static and modal analysis. In Section 4, the study examines how flexure-hinge thickness, hinge length, initial beam angle, and material properties affect the output performance of the FTS mechanism. Section 5 develops an analytical model using the PRBM to determine the stiffness and dynamic behavior. Section 6 evaluates performance results, compares analytical predictions with numerical simulations, and discusses sensitivity and parasitic motion. Finally, Section 7 summarizes the main findings and outlines future work.

2. DESIGN OF THE FULLY COMPLIANT PLANAR LINEAR-MOTION MECHANISM

2.1. Conceptual design

In this research, a fully compliant planar linear-motion mechanism was developed for integration into an FTS system used in ultra-precision diamond turning (Fig. 1). Within the diamond-turning configuration, the FTS unit is installed on the $Y-$slide of the machine tool and actuated by a PZT. The motion generated by the PZT is conveyed to the cutting tool through flexural joints, enabling rapid and highly accurate positional adjustments throughout the machining operation.

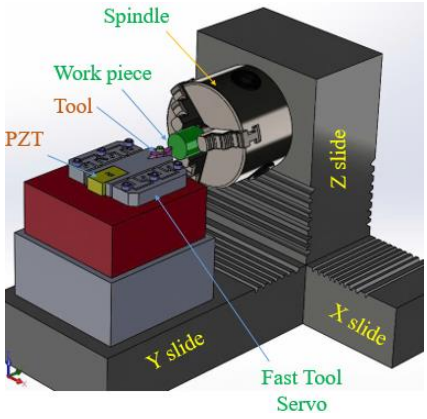

Fig. 1. A FTS system in ultra-precision diamond turning

2.2. Design parameters

The proposed mechanism utilizes the fundamental kinematic principle of the Roberts straight-line mechanism, as described by W. Chen, Jiang, Chen, and Liu (2013), W. Chen, Jiang, Liu, et al. (2013), Paniselvam et al. (2023), and Wan et al. (2016), but integrates it into a novel symmetric multi-branch configuration to enhance stiffness and dynamic performance (Figs. 2(a)–(c)). This design uses a planar monolithic structure fabricated from a single piece of material, which ensures high manufacturing accuracy, excellent geometric repeatability, and eliminates assembly errors.

The mechanism comprises the following key components:

- Piezoelectric actuator (PZT): providing the input displacement or input force.
- Roberts' straight-line mechanisms: integrated symmetrically on both sides of the central stage to guide linear motion with minimal parasitic rotation.
- Tool-holder stage: located at the top center, directly connected to the cutting tool for transferring amplified displacement to the machining point.

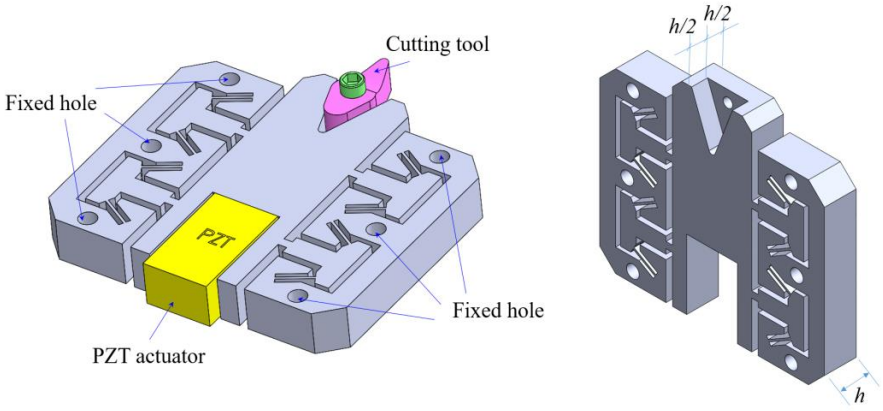

(a) (b)

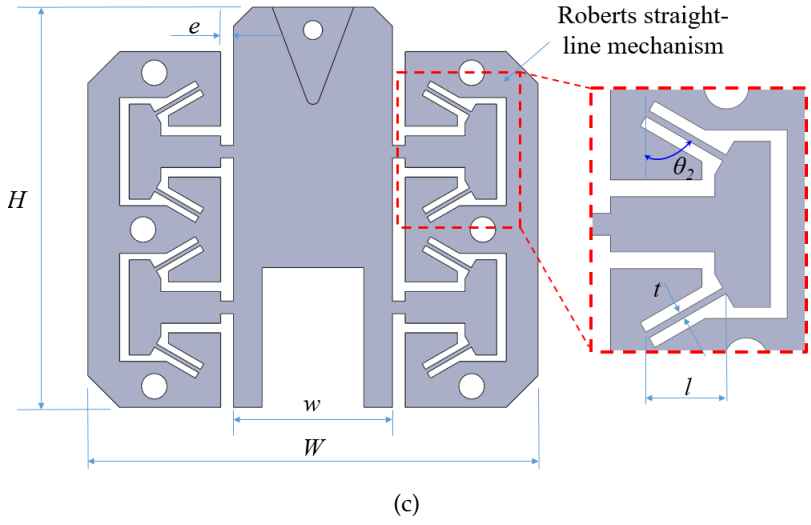

(c)

Fig. 2. Schematic diagram of the FTS

The geometry of this fully compliant, planar, linear-motion mechanism is characterized by several critical design parameters, as summarized in Table 1.

Table 1. Basic design parameters of FTS

Symbol	Descriptions	Value	Unit
h	Thickness of the mechanism	10	mm
l	Length of flexure hinge	8	mm
e	Distance between movable plate and RSM mechanism	2	mm
t	Thickness of flexure hinge	0.6	mm
θ_2	Angle of inclination of flexure hinge relative to the vertical	60	degrees
ω	Width of mobile element	25	mm
H	Overall height of the FTS	70.8	mm
W	Overall width of the FTS	63	mm
Overall dimensions of FTS: 70.8 × 63.0 × 10.0 mm			

2.3. Working principle

The proposed mechanism operates by transmitting the displacement generated by the PZT to the central moving stage through a set of symmetrically arranged compliant Roberts linkages. When the PZT expands or contracts, the input motion is delivered to the flexure hinges, causing the compliant beams within each Roberts mechanism to deform elastically. This deformation enables the coupler stage to move along a nearly straight trajectory.

The four-branch symmetric configuration plays a critical role in ensuring high translational accuracy. Each Roberts linkage contributes to motion guidance, and their symmetric placement cancels out lateral forces and rotational moments that would otherwise introduce parasitic motion. As a result, the central stage experiences predominantly unidirectional displacement with extremely low off-axis components.

During operation, the compliant beams undergo bending while the rigid sections act as transmission links that preserve kinematic relationships inherent to the Roberts mechanism. This combination allows the structure to approximate straight-line motion without the need

for sliding or rolling joints. The monolithic construction further enhances repeatability by eliminating assembly errors and frictional effects typically found in conventional guiding mechanisms.

2.4. Fabrication Considerations

The performance of flexible mechanisms often depends heavily on the precise fabrication of thin flexural hinges, which govern the stiffness and deformation of the mechanism. As reported by Chau et al. (2018), Y. Liu and Zhang (2021), and Wei et al. (2018), hinge thicknesses are typically only 0.3 to 1.5 mm; therefore, machining by conventional methods can introduce burrs, residual stresses, or geometrical deviations, which alter the stiffness and secondary motion predicted in analytical and FEM models. To achieve the required dimensional accuracy and surface quality, Miller et al. (2005) identified Wire-EDM as the preferred method due to its ability to produce high-aspect-ratio flexural hinges with minimal thermal or mechanical deformation. Alternative processes such as laser micromachining or micro-end milling can be used, but heat-affected zones or tool-induced errors must be carefully controlled, as noted by Le et al. (2025). Since the bending stiffness is proportional to approximately t^3 according to beam theory, even small changes in thickness can significantly alter the static and dynamic properties discussed in the following sections. Therefore, post-fabrication inspection is essential to ensure that the hinge dimensions conform to the design specifications and maintain the desired motion accuracy of the mechanism. Within the scope of this study, the effects of the machining method on the performance of the proposed FTS were assumed to be very small and were neglected during the FEM analysis and analytical calculations.

3. FINITE ELEMENT MODELING

FEA was conducted using ANSYS 19.2 to investigate the structural characteristics of the proposed FTS. Al7075, whose technical specifications are shown in Table 2, was selected as the structural material for the simulations.

Table 2. Specifications of Al7075, from F. Chen et al. (2025)

Yield strength (MPa)	Density (kg/m^3)	Young's modulus (MPa)	Poisson's ratio
503	2810	71,700	0.33

A small-deformation analysis was carried out to evaluate key performance indicators, including output displacement, stress distribution, and natural frequencies. The mesh was initially generated automatically and subsequently refined at critical regions, particularly near the flexure hinges, to enhance computational accuracy. The corresponding simulation parameters are summarized in Table 1. The boundary conditions were defined by constraining the holes, while an input force of 50 N was applied at the middle of the movable element. The numerical model comprised 129,385 nodes and 76,178 elements, as listed in Table 3. A medium-level mesh refinement strategy was adopted, in which coarser elements were assigned to the relatively rigid regions, and finer elements were concentrated in the deformable zones to achieve an optimal balance between accuracy and computational efficiency, as illustrated in Fig. 3.

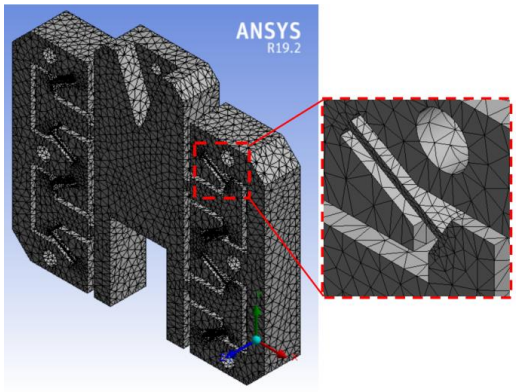

Fig. 3. Meshed model of the FTS

Table 3. Technical information on FEA

Element type	Element size (mm)	Number of Nodes	Number of Elements	Mesh quality (Smoothing)	Mesh	
					Skewness	Orthogonal Quality
					Average	
SOLID 187/Test10	1.0	129385	76178	Medium	0.45	0.55
					Standard deviation	
					0.19	0.19

The mesh quality evaluation summarized in Fig. 4(a) indicates that most deviation values range from 0.13 to 0.75, yielding a mean of approximately 0.45. According to the ANSYS mesh quality index, this range corresponds to a good quality classification (0.50–0.80). As shown in Fig. 4(b), the average orthogonal quality of 0.55 also falls comfortably within the permissible interval of 0.20–0.69, demonstrating that the element shapes are appropriate for the intended analysis. The relatively low standard deviations of both measures (∼0.2) further reflect a consistent and well-conditioned mesh free from significant distortion. The integration of localized refinement and smoothly graded transitions in highly deformable regions enhances numerical robustness. Collectively, these characteristics ensure that the finite-element model maintains the stability and precision necessary for dependable simulation outcomes, consistent with the criteria discussed by ANSYS Inc. (2013) and Ferrara-Bello et al. (2021).

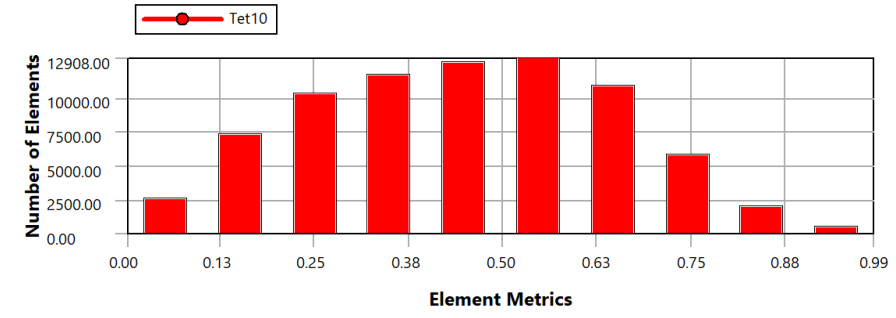

(a)

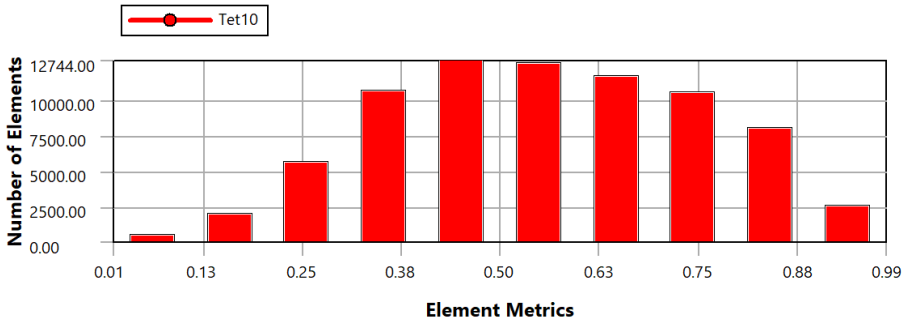

(b)

Fig. 4. Mesh metric: (a) skewness distribution; (b) orthogonality quality distributions

Under the action of the input force from the PZT actuator, the cutter moves along the Y-axis to engage the workpiece, thereby performing the cutting process and causing structural deformation in the elastic mechanism. As shown in Figs. 5 and 6, the maximum stress and strain appear at the two ends of the flexure hinge. To examine its resonance behavior, the dynamic response was analyzed, with the first six natural vibration modes and their corresponding resonance frequencies (Table 4) illustrated in Fig. 7.

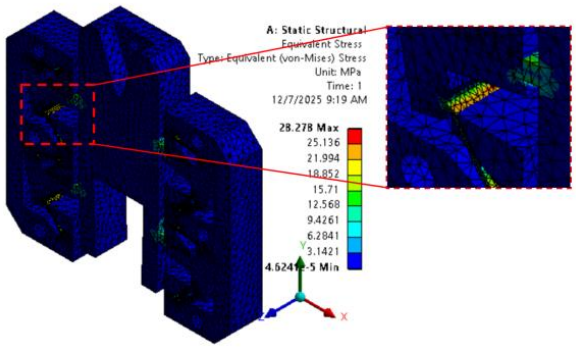

Fig. 5. Stress distribution of the FTS

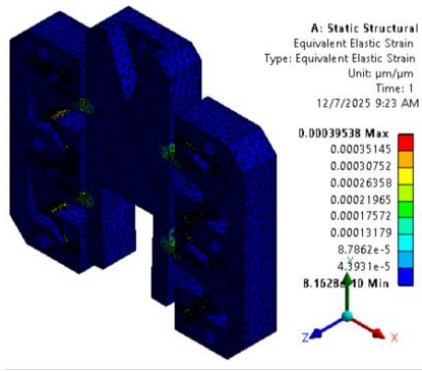

Fig. 6. Strain distribution of the FTS

Table 4. The first six modes of natural frequency of FTS

Mode	1	2	3	4	5	6
Natural frequencies (Hz)	1289.3	3282	4730.6	4966.1	7854.3	8050.1

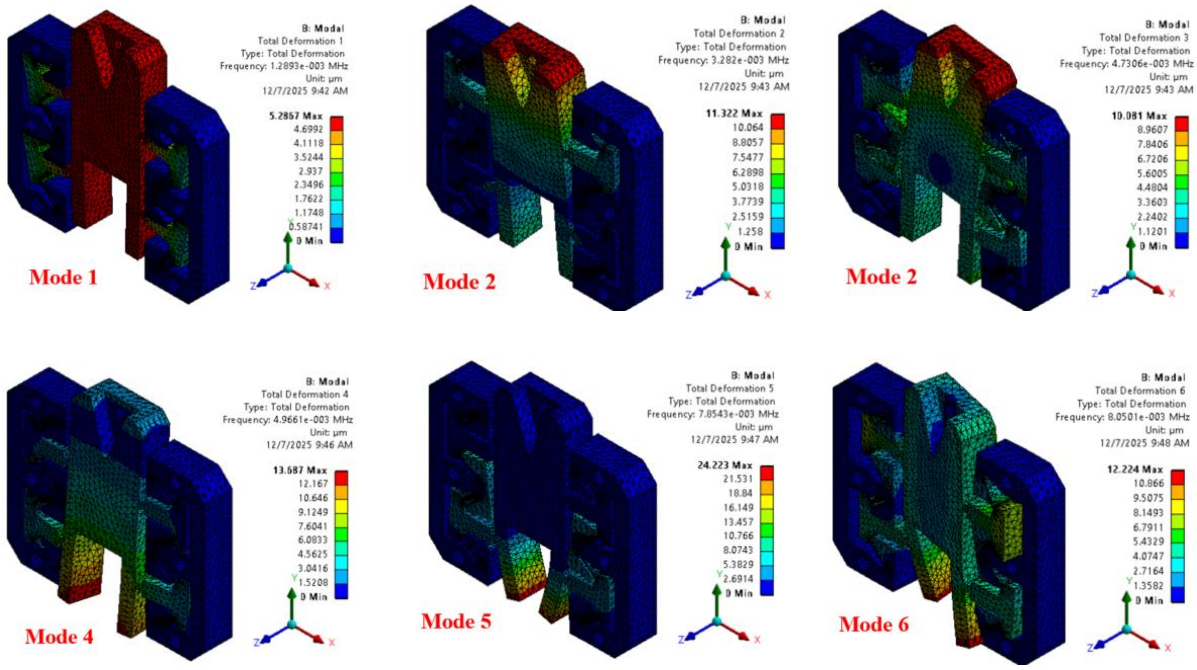

Fig. 7. The first six natural frequencies of FTS

The modal analysis reveals that the first six natural frequencies of the FTS mechanism range from 1289.3 Hz to 8050.1 Hz. The fundamental mode occurs at 1289.3 Hz, which is significantly higher than the typical excitation range observed in fast tool servo diamond turning (typically around 300-800 Hz) reported by H. Li et al. (2021), Liang et al. (2017), and Ma et al. (2013). This frequency separation suggests that the mechanism is unlikely to experience resonance during normal cutting operations. The higher-order modes, ranging from 3282 Hz to 8050.1 Hz, further indicate that the structure maintains substantial dynamic stiffness, supporting stable high-bandwidth actuation.

4. SENSITIVITY ANALYSIS

To evaluate the robustness and long-term performance of the proposed FTS mechanism, a comprehensive sensitivity analysis was undertaken. The investigation concentrated on the geometric attributes most likely to affect the output characteristics of the flexure hinge. Prior studies consistently indicate that the stiffness and dynamic response of compliant mechanisms exhibit pronounced sensitivity to hinge thickness, hinge length, and overall beam geometry. Guided by these insights, the present study selected the hinge thickness (t), hinge length (l), and the initial beam angle (θ_2) as key design variables for systematic assessment. Finite element simulations were carried out by varying each parameter individually while keeping all other geometric and material properties fixed. The resulting performance trends and comparative outcomes are summarized in Table 5.

Table 5. Sensitivity summary of the proposed compliant FTS mechanism

Parameter	Variation	Displacement (μm)	Stiffness (N/μm)	Max stress (MPa)	Natural frequency (Hz)
Hinge thickness t (mm)	0.5	24.33	2.06	30.70	1171.9
	0.6	20.26	2.47	28.30	1289.3
	0.7	16.62	3.01	25.10	1429.2
	0.8	13.63	3.67	21.80	1585.5
Hinge length l (mm)	7	17.03	2.93	27.90	1408
	8	20.26	2.47	28.30	1289.3
	9	23.15	2.12	27.70	1204.4
	10	26.08	1.89	27.40	1133.4
Initial angle θ_2 (deg)	55°	19.17	2.6	25.99	1333.2
	60°	20.26	2.46	28.30	1298.3
	65°	22.23	2.24	31.30	1222.1
	70°	23.36	2.14	32.60	1180.9
Material (E)	65Mn ($E = 211$ GPa)	7.04	7.10	28.27	1308.30
	Al7075 ($E = 71.7$ GPa)	20.26	2.47	28.30	1298.30
	Ti6Al4V ($E = 115$ GPa)	12.54	3.98	28.29	1295.00
	Stainless steel ($E = 193$ GPa)	7.61	6.57	28.27	1266.50

4.1. Effect of flexure hinge thickness

Based on Table 5, the relationship between the thickness t of the flexure hinge, the natural frequency, and the generated stress is plotted as shown in Fig. 8.

It is evident that the hinge thickness (t) has the strongest and most direct impact on both the static and dynamic characteristics of the proposed compliant FTS mechanism. As shown in Table 5 and illustrated in Fig. 8, increasing t from 0.5 mm to 0.8 mm results in a simultaneous increase in natural frequency and a decrease in maximum stress, reflecting a clear stiffness-enhancing effect. When the hinge becomes thicker, the flexure beam develops substantially larger bending rigidity, which restricts elastic deformation and consequently reduces stress concentration in the hinge region. Specifically, the maximum stress drops from 30.70 MPa at $t = 0.5$ mm to 21.80 MPa at $t = 0.8$ mm. This decreasing trend indicates a more favorable stress distribution under loading and improved structural robustness.

In contrast, the natural frequency increases monotonically from 1171.9 Hz to 1585.5 Hz as t increases. This is consistent with the dynamic behavior in compliant structures, where higher hinge stiffness leads to higher global dynamic stiffness, thereby elevating the resonant frequencies. The near-linear growth in natural frequency also demonstrates that hinge thickness is a highly effective design variable for tuning the dynamic bandwidth of the FTS mechanism.

4.2. Effect of flexure hinge length

The length of the flexure hinge (l) plays an important role in determining the compliance and deformation curvature, and consequently influences both the stress distribution and the dynamic stability of the proposed FTS mechanism. The numerical results in Table 5, together with the trends illustrated in Fig. 9, show that variations in l produce systematic changes in the natural frequency and maximum stress.

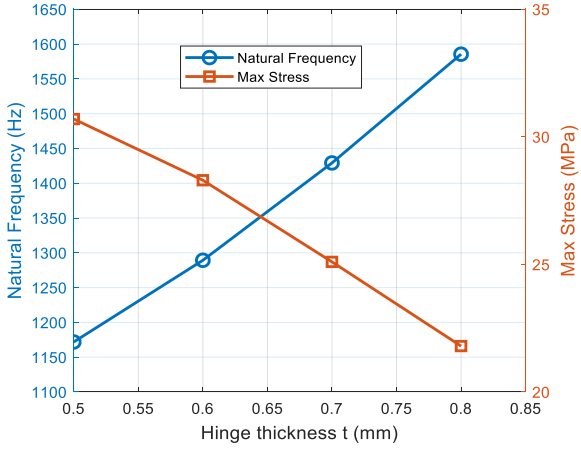

Fig. 8. The relationship between the thickness of the flexure hinge, the natural frequency and the generated stress

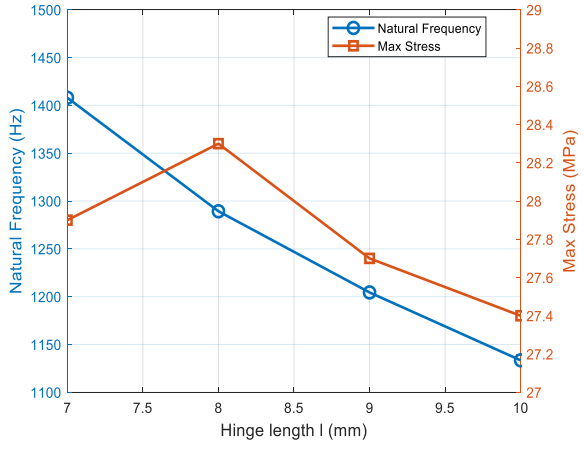

Fig. 9. The relationship between the length of the flexure hinge, the natural frequency and the generated stress

As the hinge length increases from 7 mm to 10 mm, the natural frequency decreases markedly from 1408 Hz to 1133.4 Hz. This monotonic reduction reflects the increased geometric flexibility of a longer hinge, which lowers the effective bending stiffness of the flexure and therefore reduces the dynamic stiffness of the entire mechanism. The trend indicates that l is a highly sensitive parameter for tuning the resonant behavior of the system. Short hinges favor high-bandwidth operation, while longer hinges decrease the resonant frequency and may limit the achievable tool servo speed.

The maximum stress exhibits a milder, non-monotonic variation compared with the natural frequency. As shown in Fig. 9, stress initially increases from 27.90 MPa at $l = 7$ mm to a peak of 28.30 MPa at $l = 8$ mm, followed by a gradual decrease to 27.40 MPa at $l = 10$ mm. This behavior can be attributed to the redistribution of bending curvature within the hinge. At shorter lengths, deformation is localized, resulting in higher stress gradients; increasing l reduces curvature concentration, thereby lowering peak stress. The slight rise at $l = 8$ mm is consistent with a transitional configuration where the deformation shape shifts before becoming more uniformly distributed at longer hinge lengths.

4.3. Sensitivity to initial flexure angle

The initial flexure angle θ_2 governs the geometric orientation of the compliant beams and directly affects the kinematic transmission and bending characteristics of the Roberts-based mechanism. As shown in Table 5 and Fig. 10, variations in θ_2 result in clear and systematic changes in both the natural frequency and the maximum stress.

When θ_2 increases from 55° to 70°, the natural frequency decreases from 1333.2 Hz to 1180.9 Hz. This downward trend indicates that larger inclination angles reduce the effective axial stiffness of the compliant linkage. At higher angles, the flexure beams deform with a greater lateral component, introducing additional compliance into the structure. Consequently, the system becomes dynamically softer, leading to lower resonant frequencies. This behavior shows that the initial angle is a critical parameter for tuning the dynamic bandwidth of the FTS mechanism.

Maximum stress exhibits the opposite trend: it increases steadily from 25.99 MPa at θ_2 = 55° to 32.60 MPa at θ_2 = 70°. This rise in stress is attributed to the larger bending moment induced in the flexure beams when they are oriented at steeper angles. As θ_2 increases, the deformation path becomes more curved, concentrating strain within the hinge region and elevating the peak stress value. This effect becomes more pronounced beyond 65°, where the rate of stress increase is higher.

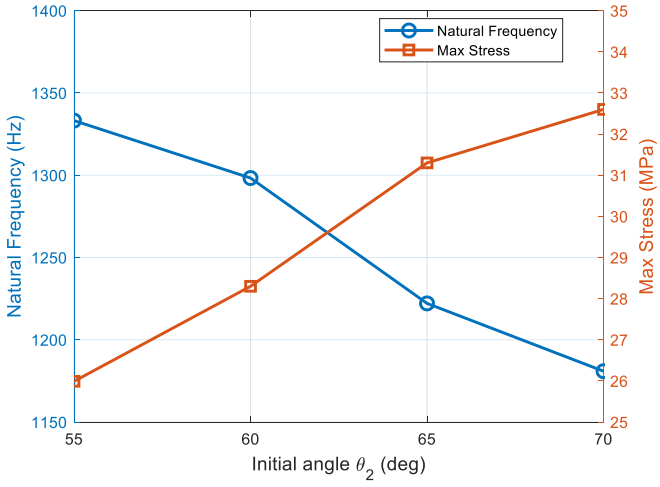

Fig. 10. The relationship between the initial angle of the flexure hinge, the natural frequency and the generated stress

4.4. Influence of material stiffness

Material stiffness, represented by Young's modulus (E), plays a central role in determining the global rigidity and deformation characteristics of the compliant mechanism. To evaluate this influence, four structural materials with distinct elastic moduli were examined: 65Mn spring

steel, Al7075, Ti6Al4V, and stainless steel. The corresponding values of displacement, stiffness, maximum stress, and natural frequency are summarized in Table 5.

The results show a clear inverse relationship between material stiffness and output displacement. Materials with higher Young's modulus, such as stainless steel (E = 193 GPa) and 65Mn (E = 211 GPa), produce significantly smaller displacements of 7.61 μm and 7.04 μm, respectively. Conversely, Al7075, with a comparatively lower modulus (E = 71.7 GPa), enables a much larger displacement of 20.26 μm. This behavior reflects the inherent reduction in compliance of stiffer materials, which limits the flexural deformation of the hinge.

Stiffness values follow the expected trend: 65Mn and stainless steel yield the highest stiffness values (7.10 N/μm and 6.57 N/μm), whereas Al7075 provides the lowest (2.47 N/μm). Ti6Al4V exhibits intermediate stiffness (3.98 N/μm) due to its medium-range elastic modulus. This demonstrates that the global stiffness of the compliant mechanism is highly sensitive to material selection and can be tuned effectively through appropriate material engineering. Maximum stress remains nearly constant across different materials ($\approx$ 28 MPa), indicating that stress levels are predominantly governed by geometric deformation rather than material stiffness. This also implies that all tested materials operate well below their yield limits under the applied loading conditions.

The natural frequency exhibits only moderate variation with material stiffness, ranging from 1266.5 Hz for stainless steel to 1308.3 Hz for 65Mn. Although the changes are moderate compared with geometric parameter variations, they confirm that material stiffness contributes to improving dynamic bandwidth.

The sensitivity study shows that hinge thickness (t) is the most influential parameter, strongly affecting stiffness, maximum stress, and natural frequency due to its dominant role in flexural rigidity. Hinge length (l) and initial angle (θ_2) have moderate but predictable effects on displacement and dynamic response, while material stiffness mainly shifts overall compliance without significantly altering stress levels. Overall, the proposed FTS mechanism demonstrates stable and consistent behavior across parameter variations, confirming its robustness and providing clear guidelines for tuning performance in high-bandwidth applications.

5. STRUCTURAL MODELING

Building on the insights obtained from the sensitivity analysis, it becomes evident that the geometric parameters of the flexure hinges play a decisive role in shaping the mechanical response of the compliant mechanism. To better understand the underlying relationships between these parameters and the resulting stiffness and dynamic characteristics, a more rigorous analytical framework is required. This section develops a detailed structural model of the proposed FTS mechanism based on the pseudo-rigid-body method and the Lagrangian equation following Ho et al. (2019). This analytical model not only clarifies the contribution of each structural component but also establishes the foundation for predicting system stiffness, equivalent mass, and natural frequency, thereby complementing and validating the numerical findings presented earlier.

5.1. Stiffness analysis

The FTS introduced in this work features an integrated configuration composed of four compliant Roberts mechanisms (Fig. 11), each governed by the kinematic principles outlined in Fig. 12. When an external force is applied to the terminal point of the coupler extension, the corresponding flexural beams experience elastic deformation, resulting in an approximately linear displacement. To characterize the stiffness behavior of the Roberts mechanism, the PRBM is adopted. This modeling framework transforms the compliant structure into an equivalent rigid-body system, where the elastic behavior of flexural elements is represented by torsional springs located at virtual joints. Such an approach enables the use of well-established rigid-body kinematic formulations for analyzing and designing compliant mechanisms. As illustrated in

Fig. 13, the PRBM of a single compliant Roberts mechanism replaces the two flexible beams with four identical torsional springs and two rigid links, effectively capturing the system's deformation characteristics. The basic design parameters of the mechanism are presented in Table 6.

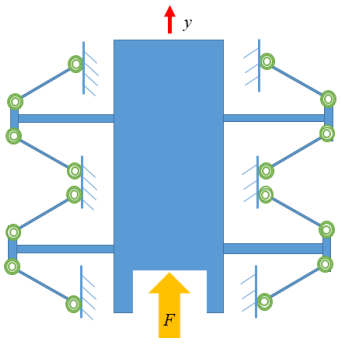

Fig. 11. The PRBM of FTS

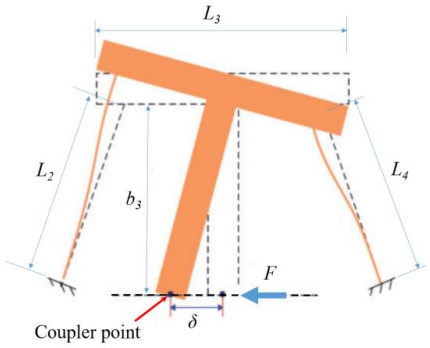

Fig. 12. An example of a compliant Roberts mechanism's operation, adapted from Wan et al. (2016)

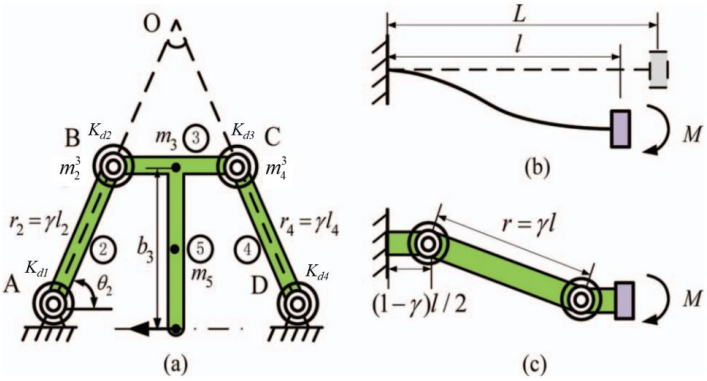

Fig. 13. (a) one Roberts mechanism's PRBM, (b) flexible beam deformation, (c) flexible beam PRBM, and (d) beam element parameters, adapted from W. Chen, Shi, et al. (2013b)

Table 6. Basic design parameters of the Roberts mechanism

Parameter	Symbol	Value	Unit
Dimensions of flexible links 2 and 4	l_2, l_4	8	mm
Dimensions of flexible links 2 and 4	h_2, h_4	10	mm
Dimensions of flexible links 2 and 4	t_2, t_4	0.6	mm
Dimensions of flexible link 3	l_3	12	mm
Dimensions of flexible link 3	h_3	10	mm
Dimensions of flexible link 3	t_3	5	mm
Dimensions of flexible link b_3	l_{b3}	12.9	mm
Dimensions of flexible link b_3	h_{b3}	10	mm
Dimensions of flexible link b_3	t_{b3}	5	mm
Link 2 and 4's initial angle	θ_{20}, θ_{40}	60°	degrees
Link 3's initial angle in joint B	θ_{30}	0°	degrees

The stiffness of the structure is determined by Hooke's law using Eq. (1):

$$K_{Syt} \approx \frac{F}{y}, \tag{1}$$

here, y denotes the displacement of the movable plate, while F represents the corresponding applied force.

The determination of these two parameters is carried out through the equations provided below:

$$y = r_2 \left(\cos\theta_2 - \cos\theta_{20}\right) + b_3 \sin\theta_3 + \frac{r_3}{2}\left(\cos\theta_3 - 1\right), \tag{2}$$

$$F = N_T K_\psi \times \frac{\left(h_{32} - 2\right)\Delta\theta_2 + \left(h_{32} - 2h_{42}\right)\Delta\theta_4 + \left(1 + h_{42} - 2h_{32}\right)\Delta\theta_3}{r_2 \sin\theta_2 + h_{32}\left(\frac{r_3}{2}\sin\theta_3 - b_3\cos\theta_3\right)}, \tag{3}$$

where θ_{i0}, θ_i, and $\delta\theta_i (i = 2, 3, 4)$ denote, respectively, the initial angle, the maximum angular position, and the corresponding angular variation of link i. The variable r_i represents the length of link i, while b_i defines the minimum distance from the centroid of link 3 to its associated joint. The parameter N_t designates the total number of Roberts mechanisms employed in the configuration, which is four in the present study. The torsional spring constant, K_Φ, is evaluated using the following governing equation

$$h_{32} = \frac{\delta\theta_3}{\delta\theta_4} = \frac{r_2 \sin\left(\theta_4 - \theta_2\right)}{r_3 \sin\left(\theta_3 - \theta_4\right)}, \tag{4}$$

$$h_{42} = \frac{\delta\theta_4}{\delta\theta_2} = \frac{r_2 \sin\left(\theta_3 - \theta_2\right)}{r_4 \sin\left(\theta_3 - \theta_4\right)}, \tag{5}$$

and

$$K_\psi = 2\gamma K_\phi \frac{EI}{l}, \quad I = \frac{ht^3}{12}. \tag{6}$$

In the formulation of the PRBM, the parameter γ denotes the characteristic radius factor, whereas K_ϕ represents the rotational stiffness coefficient. Following Wan and Xu (2016), these parameters are approximated as 0.852 and 2.65, respectively.

5.2. Equivalent mass analysis

Within the PRBM framework, a single compliant Roberts mechanism is abstracted as a system comprising four identical torsional spring elements ($K_{d1} = K_{d2} = K_{d3} = K_{d4}$) and two lumped masses equivalent to the flexible members ($m_2^3 = m_4^3$), as depicted in Fig. 13(a).

Given that $m_2 = m_4$, $J_2 = J_4$, and $r_2 = r_4$, the parameter lm_2 can be expressed as follows:

$$J_i = \frac{1}{12} m_i l_i^2, \tag{7}$$

$$lm_2 = lm_4 = \frac{1}{4} m_2 + \frac{J_2}{r_2^2}. \tag{8}$$

The masses m_2 and m_4 are determined using the expression $m_2 = m_4 = l \times t \times h \times \rho$, where ρ represents the material's density.

The kinetic energy of the PRBM system can be formulated as follows:

$$T = \frac{1}{2} m_R u^2 = \frac{1}{2} m_2^3 v_B^2 + \frac{1}{2} m_4^3 v_C^2 + \left(\frac{1}{2} m_3 v_{m3}^2 + J_3 \omega_3^2\right) + \left(\frac{1}{2} m_{b3} v_{b3}^2 + J_{b3} \omega_3^2\right). \tag{9}$$

In this model, m_R denotes the equivalent mass corresponding to a single compliant Roberts mechanism, while m_i and J_i represent the mass and mass moment of inertia of link $i (i = 3, b_3)$, respectively. The lumped masses attributed to the two flexible members are reported by W. Chen, Jiang, Liu, et al. (2013). Moreover, u designates the velocity of the coupling point, ω_3 the angular velocity of link 3, and v_B, v_C, v_{m3}, and v_{b3} the linear velocities of their associated points.

From the classical kinematic formulation of rigid-body motion in a four-bar linkage, it is well recognized that:

$$v_B = v_C = f(\theta_2, u),\ v_{m3} = g(\theta_2, u),\ v_{b3} = h(\theta_2, u),\ \text{and}\ \omega_3 = q(\theta_2, u). \tag{10}$$

Consequently, the equivalent mass corresponding to an individual Roberts mechanism can be determined as follows:

$$m_R = \alpha\left(m_2^3 + m_4^3\right) + \beta m_3 + \psi m_{b3} + \frac{1}{\chi^2}\left(J_3 + J_{b3}\right), \tag{11}$$

where

$$\chi = \frac{r_3}{2} tg\theta_2 + b_3, \quad \alpha = \frac{r_3^2}{4\chi^2 \cos^2\theta_2}, \quad \beta = \left(1 - \frac{b_3}{\chi}\right)^2, \text{ and } \psi = \left(1 - \frac{b_3}{2\chi}\right)^2. \tag{12}$$

The equivalent mass of the system is given by:

$$M_{Syt} = 4m_R + m_{mov}, \tag{13}$$

where m_{mov} is the mass of the movable plate calculated as described by Ho et al. (2019).

5.3. Dynamic modeling

The Lagrange equation of Ho et al. (2019) is used to describe the free oscillation of the FTS mechanism; the governing equation is defined as follows:

$$M_{Syt}\ddot{y} + K_{Syt}y = 0, \tag{14}$$

where $\ddot{y}$ and y are the input displacement and the acceleration, respectively; M_{Syt} and K_{Syt} are the equivalent mass and stiffness of the FTS.

Solving Eq. (14), the natural frequency of the FTS is obtained by:

$$f = \frac{1}{2\pi}\sqrt{K_{Syt}/M_{Syt}}. \tag{15}$$

6. PERFORMANCE EVALUATION

After the structural characteristics of the FTS mechanism are established through both analytical modeling and parametric sensitivity analysis, this section evaluates the performance of the FTS under representative loading conditions. While the previous sections have clarified how geometric and material parameters affect stiffness and dynamic behavior, the current analysis focuses on quantifying the responses of the mechanism when subjected to external forces.

To perform this analysis, the optimal design parameters listed in Table 1 were used, and a series of finite element simulations was performed to examine the relationship between the applied input force and the tool displacement. To ensure the stability of the analysis, the input force was varied from 1 N to 15 N, and the output responses and generated stresses were recorded. The numerical results are summarized in Table 7 and illustrated in Fig. 14.

The results presented in Table 7 and Fig. 14 demonstrate a distinct linear correlation between the input force and the output displacement of the FTS mechanism. As the input force increases from 1 N to 15 N, the output displacement proportionally rises from 0.40 µm to 6.07 µm, confirming that the mechanism exhibits stable elastic behavior throughout the tested force range. Additionally, parasitic motion increases slightly with the applied force, reaching 0.0011 µm at 15 N. However, the ratio of parasitic motion to output displacement remains nearly constant at approximately 0.02%, indicating that parasitic motion scales proportionally with the main displacement. The extremely low ratio ($< 0.1\%$) verifies the mechanism's excellent directional motion capability with minimal undesired movement.

Table 7 also reveals that the stiffness of the mechanism remains nearly constant at 2.46 N/µm under all loading conditions. This consistent stiffness behavior indicates predictable

and reliable mechanical performance, which is essential for high-precision applications. The stress analysis further supports the structural soundness of the design: the maximum stress generated under a 15 N input force is 8.5 MPa, far below the allowable stress limit of the AL7075 material (503 MPa), demonstrating a high safety margin and ensuring long-term durability and reliability.

Table 7. Static performance analysis of the FTS mechanism

Input Force (N)	Output displacement (μm)	Stress (MPa)	Parasitic motion Parasitic motion (μm)	Ratio (%)	Stiffness of FTS (N/μm)
1	0.40	0.6	0.0001	0.02	2.46
3	1.21	1.7	0.0002	0.02	2.46
6	2.43	3.4	0.0004	0.02	2.46
9	3.64	5.1	0.0007	0.02	2.46
12	4.86	6.8	0.0009	0.02	2.46
15	6.07	8.5	0.0011	0.02	2.46

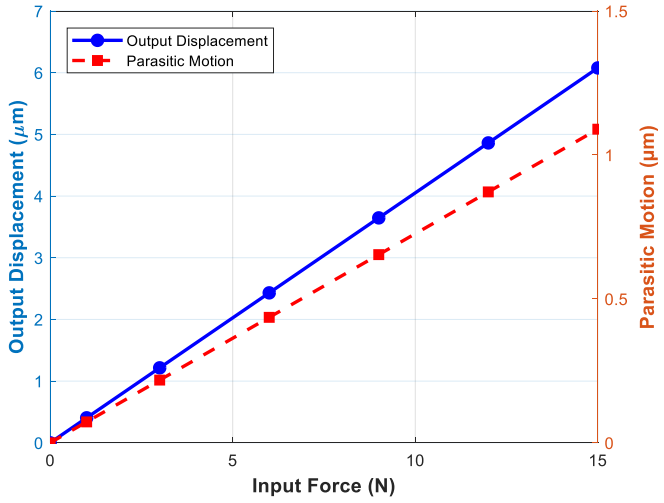

Fig. 14. Relationship between input force, output displacement, and parasitic motion

As illustrated in Fig. 14, both the output displacement and parasitic motion increase simultaneously, yet the slope of the output displacement curve is significantly steeper. This indicates that the desired motion strongly dominates over the parasitic component, thereby confirming the superior motion accuracy of the mechanism and its suitability for precision engineering applications.

To further substantiate the validity of the proposed design and its analytical modeling, a quantitative comparison between theoretical predictions and numerical simulations was conducted. Table 8 presents a comparative analysis of stiffness and natural frequency values obtained from both FEM simulations and theoretical calculations. Noticeable discrepancies are observed between the two methods: the FEM predicts a stiffness of 2.46 N/μm, which is approximately 15.72% higher than the theoretical value of 2.08 N/μm. Similarly, the FEM-derived natural frequency of 1289.3 Hz exceeds the theoretical estimate of 1171.07 Hz by 10.10%. These deviations emphasize the inherent limitations of analytical models in accurately representing the detailed structural responses that can be captured by FEM simulations. The discrepancies primarily originate from simplifying assumptions in the theoretical formulations, such as

idealized geometry, homogeneous material properties, mesh sizes, and restricted boundary conditions or degrees of freedom. Nevertheless, the magnitude of the observed errors falls within an acceptable range and aligns well with the deviations reported by W. Chen, Shi, et al. (2013b), Lai et al. (2012), Y. Li and Xu (2011), and Wan and Xu (2016), thereby validating the reliability of both the theoretical and numerical approaches.

Table 8. Error analysis of stiffness and frequency between FEM and theoretical models

Model	Stiffness (N/μm)	Frequency (Hz)
FEM analysis results	2.46	1289.30
Theoretical analysis results	2.08	1171.07
Error between FEM and theory (%)	15.72	10.10

The acceptable agreement between the FEM results and the theoretical results in Table 8 confirms that the approach used in this study provides a relatively accurate description of the FTS behavior. This agreement establishes a reliable basis for evaluating the practical performance of the design.

In addition to this verification, the comparison of the proposed FTS mechanism with previously published designs helps to support the reliability of the approach. For this purpose, Table 9 summarizes a comparative performance analysis including key metrics such as natural frequency, stiffness, travel capacity, and parasitic motion. By placing the present results next to previous representative works, it is clear that the proposed mechanism achieves a well-balanced combination of high dynamic bandwidth, adequate stiffness, and low parasitic motion. These comparison results demonstrate that the proposed design is not only competitive but also well suited for fast tool servo applications requiring high precision, stability, and frequency performance.

Table 9. Performance comparison with existing compliant FTS designs

Work	Parasitic (%)	Natural frequency (Hz)	Stiffness (N/μm)	Stroke (μm)
Liang et al. (2017)	-	316.84	-	258.3
Yong (2020)	0.03	-	8.28	1000
Zhao et al. (2023)	-	1250	48.08	15
J. Liu et al. (2022)	0.174	956.21	2.748	36.39
Wu et al. (2025)	-	1160.75	3.37	39.79
This work	$<$ **0.02**	**1289**	**2.47**	**6**

Furthermore, Y. Chen et al. (2017) reported that, in ultra-precision diamond turning, the material removal rate is extremely small and the corresponding cutting forces typically range from only a few tens to a few hundreds of millinewtons. Hence, as indicated by Zhou et al. (2022), an operational load capacity of approximately 5 N is generally sufficient for practical micro-cutting conditions and provides a broad safety margin for flexure-based structures. To further verify the robustness of the proposed mechanism, an axial Z-direction load of 15 N, substantially higher than typical micro-cutting thrust forces, was applied at the tool tip in an auxiliary FEM simulation. The resulting maximum von Mises stress was only 5.42 MPa, which is far below the yield strength of Al7075 (503 MPa) and even lower than the stress levels observed under the primary Y-direction actuation. These results confirm that axial cutting loads do not pose any structural risk to the mechanism and that the proposed compliant FTS maintains fully elastic behavior under both nominal and worst-case micro-cutting conditions.

7. CONCLUSIONS

This study presented the design, modeling, and performance evaluation of a symmetric, fully compliant Roberts-based linear guide tailored for high-frequency FTS applications. Leveraging a four-branch symmetric configuration, the proposed mechanism enables highly accurate linear motion with substantial suppression of parasitic errors while maintaining compactness and structural integrity. The compliant Roberts-based topology demonstrated clear advantages in stiffness uniformity, motion accuracy, and dynamic robustness compared with conventional flexure-based FTS designs.

A comprehensive analytical framework based on the PRBM and Lagrangian dynamics was developed to estimate the stiffness, equivalent mass, and natural frequency of the mechanism. The analytical predictions showed good agreement with the FEA results, with deviations of 15.72% in stiffness and 10.10% in natural frequency, well within the acceptable range for compliant mechanism modeling. This consistency confirms the validity of the theoretical model and its suitability for preliminary design and optimization.

Performance evaluation revealed that the mechanism exhibits a highly linear force–displacement relationship, with a constant stiffness of approximately 2.46 N/μm. The parasitic motion remained extremely low ($< 0.02\%$), verifying the effectiveness of the symmetric multi-branch architecture in suppressing undesired lateral and rotational components. Moreover, the maximum stress under operational loading was only 8.5 MPa, substantially below the yield strength of Al7075, indicating a high safety margin and excellent structural durability. The first natural frequency reached 1289 Hz, surpassing most compliant FTS mechanisms reported in the literature and satisfying the requirements for high-bandwidth diamond turning.

A comparison with existing designs further demonstrated that the proposed mechanism achieves a balanced combination of high dynamic bandwidth, low parasitic error, and competitive stiffness, positioning it as a strong candidate for next-generation ultra-precision FTS platforms. These results confirm that symmetric compliant Roberts-based mechanisms hold significant potential for high-frequency, high-accuracy machining applications. Future work will focus on multi-objective geometric optimization to enhance bandwidth and displacement performance, prototype fabrication followed by experimental validation, and integration with real-time sensing and control strategies to enable closed-loop operation in ultra-precision diamond turning.

DECLARATION OF COMPETING INTEREST

The authors declare that they have no known competing financial interests or personal relationships that could have appeared to influence the work reported in this paper.

CREDIT AUTHOR STATEMENT

Tan Thang Nguyen: *Investigation. Software, Validation, Writing - original draft*. Thanh-Phong Dao and Hieu Giang Le: *Conceptualization, Methodology, Project administration, Funding acquisition*. Nhat Linh Ho: *Supervision, Writing - review & editing*.

FUNDING

This research is funded by the Vietnam National Foundation for Science and Technology Development (NAFOSTED) under Grant number 107.01-2024.01.

ACKNOWLEDGEMENT

The authors acknowledge HUTECH University and Ho Chi Minh City University of Technology and Engineering for supporting this study.

REFERENCES

Abdulkadir, L., Abou-El-Hossein, K., Jumare, A., Odedeyi, P., Liman, M., & Olaniyan, T. (2018). Ultra-precision diamond turning of optical silicon-a review. *The International Journal of Advanced Manufacturing Technology*, *96*(1-4), 173–208. https://doi.org/10.1007/s00170-017-1529-x

ANSYS Inc. (2013). *Introduction to ansys meshing*.

Chau, N. L., Dao, T., & Nguyen, V. T. (2018). An efficient hybrid approach of finite element method, artificial neural network-based multiobjective genetic algorithm for computational optimization of a linear compliant mechanism of nanoindentation tester. *Mathematical Problems in Engineering*, *2018*, 1–19. https://doi.org/10.1155/2018/7070868

Chen, F., Zhou, Y., Zhong, L., Yang, W., & Gan, J. (2025). Design of a strain gauge-based force sensor with three ranges based on compliant mechanisms. *IEEE Transactions on Instrumentation and Measurement*, *74*, 1–10. https://doi.org/10.1109/tim.2025.3529078

Chen, W., Jiang, J., Chen, W., & Liu, J. (2013). A novel flexure-based uniaxial force sensor with large range and high resolution. *Science China Technological Sciences*, *56*(8), 1940–1948. https://doi.org/10.1007/s11431-013-5240-3

Chen, W., Jiang, J., Liu, J., Bai, S., & Chen, W. (2013). A passive eddy current damper for vibration suppression of a force sensor. *Journal of Physics D: Applied Physics*, *46*(7), 075001. https://doi.org/10.1088/0022-3727/46/7/075001

Chen, W., Shi, X., Chen, W., & Zhang, J. (2013a). A two degree of freedom micro-gripper with grasping and rotating functions for optical fibers assembling. *Review of Scientific Instruments*, *84*(11), 1–10. https://doi.org/10.1063/1.4832045

Chen, W., Shi, X., Chen, W., & Zhang, J. (2013b). A two degree of freedom micro-gripper with grasping and rotating functions for optical fibers assembling. *Review of Scientific Instruments*, *84*(11), 1–10. https://doi.org/10.1063/1.4832045

Chen, Y., Cai, Y., Tohyama, K., Shimizu, Y., Ito, S., & Gao, W. (2017). Auto-tracking single point diamond cutting on non-planar brittle material substrates by a high-rigidity force controlled fast tool servo. *Precision Engineering*, *49*, 253–261. https://doi.org/10.1016/j.precisioneng.2017.02.014

Cheung, C., & Lee, W. (2000). Modelling and simulation of surface topography in ultra-precision diamond turning. *Proceedings of the Institution of Mechanical Engineers, Part B: Journal of Engineering Manufacture*, *214*(6), 463–480. https://doi.org/10.1243/0954405001517775

Ferrara-Bello, A., Vargas-Chable, P., Vera-Dimas, G., Vargas-Bernal, R., & Tecpoyotl-Torres, M. (2021). Xyz micropositioning system based on compliance mechanisms fabricated by additive manufacturing. *Actuators*, *10*(4), 68. https://doi.org/10.3390/act10040068

Ho, N. L., Dao, T.-P., Le Chau, N., & Huang, S.-C. (2019). Multi-objective optimization design of a compliant microgripper based on hybrid teaching learning-based optimization algorithm. *Microsystem Technologies*, *25*(5), 2067–2083.

Howell, L. L. (2001). *Compliant mechanisms* (1st ed.). John Wiley. https://doi.org/10.1007/978-94-017-9780-1_302

Hubbard, N., Wittwer, J., Kennedy, J., Wilcox, D., & Howell, L. (2004). A novel fully compliant planar linear-motion mechanism. *ASME International Design Engineering Technical Conferences*, 1–5. https://doi.org/10.1115/detc2004-57008

Lai, L., Gu, G., & Zhu, L. (2012). Design and control of a decoupled two degree of freedom translational parallel micro-positioning stage. *Review of Scientific Instruments*, *83*(4), 1–17. https://doi.org/10.1063/1.3700182

Le, H. G., Ho, N. L., & Dao, T.-P. (2025). Design synthesis, modeling, control strategies, and fabrication methods of compliant grippers for micromanipulation and micromanipulator: A comprehensive review. *Robotics and Computer-Integrated Manufacturing*, *92*, 102893. https://doi.org/10.1016/j.rcim.2024.102893

Li, H., Tang, H., Li, J., & Chen, X. (2021). Design, fabrication, and testing of a 3-dof piezo fast tool servo for microstructure machining. *Precision Engineering*, *72*, 756–768. https://doi.org/10.1016/j.precisioneng.2021.07.015

Li, Y., & Xu, Q. (2011). A totally decoupled piezo-driven xyz flexure parallel micropositioning stage for micro/nanomanipulation. *IEEE Transactions on Automation Science and Engineering*, *8*(2), 265–279. https://doi.org/10.1109/tase.2010.2077675

Li, Z., Guan, C., Dai, Y., Xue, S., & Yin, L. (2021). Comprehensive design method of a high-frequency-response fast tool servo system based on a full-frequency error control algorithm. *Micromachines*, *12*(11), 1354. https://doi.org/10.3390/mi12111354

Liang, H., Tang, H., Huang, L., Gao, J., Chen, X., & To, S. (2017). A large-stroke flexure fast tool servo with new displacement amplifier. *2017 IEEE International Conference on Advanced Intelligent Mechatronics (AIM)*, 52–57. https://doi.org/10.1109/aim.2017.8013994

Liu, J., Luo, T., Liu, K., Lai, T., Zhao, Y., & Wang, L. (2022). A novel fast servo tool device with double piezoelectric driving. *Micromachines*, *14*(1), 85. https://doi.org/10.3390/mi14010085

Liu, Y., & Zhang, Z. (2021). A large range compliant xy nano-manipulator with active parasitic rotation rejection. *Precision Engineering*, *72*, 640–652. https://doi.org/10.1016/j.precisioneng.2021.07.008

Ma, H., Tian, J., & Hu, D. (2013). Development of a fast tool servo in noncircular turning and its control. *Mechanical Systems and Signal Processing*, *41*, 705–713. https://doi.org/10.1016/j.ymssp.2013.08.011

Miller, S., Kao, C., Shih, A., & Qu, J. (2005). Investigation of wire electrical discharge machining of thin cross-sections and compliant mechanisms. *International Journal of Machine Tools and Manufacture*, *45*(15), 1717–1725. https://doi.org/10.1016/j.ijmachtools.2005.03.003

Mishra, V., Garg, H., Karar, V., & Khan, G. (2019). Ultra-precision diamond turning process. In *Ultra-precision machining processes*. Springer International Publishing. https://doi.org/10.1007/978-3-319-99900-5_4

Paniselvam, V., Jin Tan, N. Y., & Anantharajan, S. K. (2023). A review on the design and application of compliant mechanism-based fast-tool servos for ultraprecision machining. *Machines*, *11*(4), 450.

Tian, F., Yin, Z., & Li, S. (2015). Fast tool servo diamond turning of optical freeform surfaces for rear-view mirrors. *The International Journal of Advanced Manufacturing Technology*, *80*(9-12), 1759–1765. https://doi.org/10.1007/s00170-015-7152-9

Tian, F., Yin, Z., & Li, S. (2016). A novel long range fast tool servo for diamond turning. *The International Journal of Advanced Manufacturing Technology*, *86*(5-8), 1227–1234. https://doi.org/10.1007/s00170-015-8282-9

To, S., Kwok, T., Cheung, C., & Lee, W. (2006). Study of ultra-precision diamond turning of a microlens array with a fast tool servo system. In L. Yang, S. Wen, Y. Chen, & E.-B. Kley (Eds.), *2nd international symposium on advanced optical manufacturing and testing technologies: Advanced optical manufacturing technologies* (61490S, Vol. 6149). SPIE. https://doi.org/10.1117/12.674215

Wan, S., & Xu, Q. (2016). Design and analysis of a new compliant xy micropositioning stage based on roberts mechanism. *Mechanism and Machine Theory*, *95*, 125–139. https://doi.org/10.1016/j.mechmachtheory.2015.09.003

Wan, S., Zhang, Y., & Xu, Q. (2016). Design and development of a new large-stroke xy compliant micropositioning stage. *Proceedings of the Institution of Mechanical Engineers, Part C: Journal of Mechanical Engineering Science*, *231*(17), 3263–3276. https://doi.org/10.1177/0954406216643341

Wang, R., Zhang, X., & Yin, Z. (2018). Design and stiffness modeling of a compact 3-dof compliant parallel nanopositioner for the tool servo of the ultra precision machining. *2018 IEEE*

International Conference on Robotics and Biomimetics (ROBIO), 964–971. https://doi.org/10.1109/robio.2018.8664908

Wei, H., Wang, L., Niu, X., Zhang, J., & Simeone, A. (2018). Fabrication, experiments, and analysis of an lbm additive-manufactured flexure parallel mechanism. *Micromachines*, *9*(11), 572. https://doi.org/10.3390/mi9110572

Wu, L., Wang, H., Zhang, G., & Wu, S. (2025). Research on the design and control of a fast tool servo system based on a piezoelectric actuator. *The International Journal of Advanced Manufacturing Technology*, *138*(11-12), 5685–5703. https://doi.org/10.1007/s00170-025-15807-1

Yang, X., & Zhu, W. (2020). Design, analysis, and test of a novel self-sensing fast tool servo. *IEEE Transactions on Industrial Informatics*, *16*(7), 4447–4455. https://doi.org/10.1109/tii.2019.2945360

Yong, J. (2020). Design of high-performance fast tool servo system based on two-way piezoelectric ceramics. *Proceedings of the 2020 the 7th International Conference on Automation and Logistics (ICAL)*, 69–75. https://doi.org/10.1145/3412953.3412971

Zhao, D., Du, H., Wang, H., & Zhu, Z. (2023). Development of a novel fast tool servo using topology optimization. *International Journal of Mechanical Sciences*, *250*, 108283. https://doi.org/10.1016/j.ijmecsci.2023.108283

Zhou, R., Zhu, Z., Kong, L., Yang, X., Zhu, L., & Zhu, Z. (2022). Development of a high-performance force sensing fast tool servo. *IEEE Transactions on Industrial Informatics*, *18*(1), 35–45. https://doi.org/10.1109/tii.2021.3051068

Zhu, L., Li, Z., Fang, F., Huang, S., & Zhang, X. (2018). Review on fast tool servo machining of optical freeform surfaces. *The International Journal of Advanced Manufacturing Technology*, *95*(5-8), 2071–2092. https://doi.org/10.1007/s00170-017-1271-4

Zhu, Z., Chen, L., Huang, P., Schönemann, L., Riemer, O., & Yao, J. (2020). Design and control of a piezoelectrically actuated fast tool servo for diamond turning of microstructured surfaces. *IEEE Transactions on Industrial Electronics*, *67*(8), 6688–6697. https://doi.org/10.1109/tie.2019.2937051